Deformation and Fracture of Miniature Tensile Bars with Resistance-Spot-Weld Microstructures

WEI TONG, HONG TAO, XIQUAN JIANG, NIAN ZHANG, MANUEL P. MARYA, LOUIS G. HECTOR, Jr., and XIAOHONG Q. GAYDEN

Plastic deformation of miniature tensile bars generated from dual-phase steel weld microstructures (*i.e.*, fusion zone, heat-affected zone, and base material) was investigated up to final rupture failure. Uniaxial tensile true stress-strain curves beyond diffuse necking were obtained with a novel strain-mapping technique based on digital image correlation (DIC). Key microstructural features (including defects) in each of these three metallurgical zones were examined to explore the material influence on the plastic deformation and failure behavior. For weld fusion zones with minimal defects, diffuse necking was found to begin at 6 pct strain and continue up to 55 to 80 pct strain. The flow stresses of the weld fusion zones were at least twice those of the base material, and fracture strains exceeded 100 pct for both materials. The heat-affected zones exhibited a range of complex deformation behaviors, as expected from their microstructural variety. Only those fusion zones with substantial defects (*e.g.*, shrinkage voids, cracks, and contaminants) failed prematurely by edge cracking, as signaled by their highly irregular strain maps.

I. INTRODUCTION

Due to the combination of high strength and ductility, dual-phase steels are being actively investigated for future automotive applications.[1] The term "dual-phase steel" refers to the predominance of two phases in the ferrous microstructure, *viz.*, the relatively soft body-centered-cubic ferrite, and the relatively hard body-centered-tetragonal martensite. The beneficial ferrite + martensite mixture in dual-phase steels is typically produced after annealing in the so-called inter-critical temperature range, where ferrite and austenite are stabilized. This annealing is immediately followed by rapid cooling (or quenching)[2] to transform the austenite into martensite by displacement. To create adequate compromises on strength and ductility, dual-phase steels are fabricated with fine ferrite grains decorated with various amounts of coarse, segmented-looking martensite islands. Compared to precipitation-strengthened or solid-solution-strengthened low-alloy[3] steels, dual-phase steels possess a slightly lower initial yield strength (YS), a continuous flow behavior due to sufficient active slip systems in the ferrite phase, and a more uniform and higher total elongation.[1] These last two properties explain the good formability of the dual-phase steels which, when combined with high strength, have made them appealing to the automotive industry. Like other automotive materials, dual-phase steels must be resistance spot weldable, meaning that welds fabricated in these new automotive materials must fulfill a range of requirements.

Of all joining processes, resistance spot welding is the most established in the automotive industry, where it has been used for decades to join steel sheets.[4,5] In this robust process, high electrical currents are forced between two axisymmetric copper-based electrodes such that sufficient resistance heating is generated at the contacting interfaces of overlapping sheets, to melt and solidify mixed volumes of the various sheets within a fraction of a second. Due to the rapid heating and subsequent cooling, weld microstructures are considerably different from pre-existing microstructures.[4–7] In dual-phase steels, strengthening occurs in most of the weld joint as the overall fraction of martensite is dramatically increased. In steels, the extent of this microstructural strengthening, as well as the presence of solidification-induced defects (*e.g.*, voids and cracks), depends mainly upon chemical composition and, to some extent, upon the initial microstructure for a given welding condition.[8,9,10] At least three heterogeneous metallurgical zones can be distinguished in steel welds.[4,5] These are: the weld fusion zone (where melting and solidification occur); the heat-affected zone (where only solid-state phase transformations or grain growth occurs); and the unaffected base material (where temperatures are too low to alter the microstructure noticeably). The significant variations of material and mechanical properties from one zone to the other, as well as across a particular zone,[3,6,7] render extremely challenging the optimization of the welding processing parameters and the development of material models capable of capturing the complex behavior of welds.

To date, the microstructural diversity of weld joints has not been carefully considered in the deformation and fracture analysis of spot welds in crash simulation codes. Spot welds are typically represented by homogeneous beams programmed to fracture after a critical force has been locally achieved. The fracture criterion, composed of several components (normally six, for the six degrees of freedom), is calibrated from data compiled during the testing of weld coupons under various mechanical loading conditions. While such tests offer useful information on the performance of

WEI TONG, Associate Professor, HONG TAO and NIAN ZHANG, Graduate Students, and XIQUAN JIANG, Postdoctoral Fellow, are with the Department of Mechanical Engineering, Becton Engineering Center, Yale University, New Haven, CT 06520-8284. Contact e-mail: wei.tong@yale.edu MANUEL P. MARYA, formerly Researcher, Department of Metallurgical and Materials Engineering, Colorado School of Mines, is Senior Materials Engineer, NanoCoolers Inc., Austin, TX 78735. LOUIS G. HECTOR, Jr. and XIAOHONG Q. GAYDEN, Staff Research Scientists, are with the Materials and Processes Lab, General Motors R&D Center, Warren, MI 48090-9055.
Manuscript submitted October 15, 2004.

welds, they do not provide local properties at weld joints, even using reverse engineering methods. In one of these methods, finite element analysis results must be compared and matched to the experimental results of the overall load-displacement responses.[11,12,13] Although attractive, these global methods are often limited by the fact that the derived material properties can hardly be separated from empirical factors. The mechanical properties of the various weld zones must therefore be accurately quantified over a range of length scales that are compatible with those of the microstructures of spot-weld joints to improve the weld joint performance as well as the predictability of current and future numerical tools.

The small size of resistance spot welds (typically about 6 to 7 mm in diameter), and in particular the size of each heat-affected zone (typically about 0.5 to 0.7 mm wide), introduces unique experimental challenges for materials testing. To account for the various metallurgical zones and to measure the extent of changes introduced by welding, indentation tests are routinely employed. These tests provide useful estimates of local mechanical properties, particularly using well established hardness/flow stress correlations.[14,15,16] Nevertheless, indentation tests are not designed to replace the extensive data obtained from tensile tests, for material properties at large strains up to fracture. Only specific points on the measured uniaxial stress-strain curves (*e.g.*, the 8 pct strain) can be benchmarked against hardness values measured with indentation techniques, thereby demonstrating the usefulness of both methodologies. One approach to the tensile testing of spot-weld materials is to use submillimeter miniature specimens,[17] but the direct measurement of the deformation of miniature tensile specimens using the conventional clip-gage technique is difficult. Furthermore, dual-phase steel materials in both fusion weld and heat-affected zones exhibit increased strength but reduced strain-hardening rates, which leads to the onset of diffuse necking at the very early stage of a uniaxial tensile test. The conventional uniaxial tensile test methodology, based on the average deformation over the entire gage section of a tensile coupon, is not designed to measure the material deformation behavior beyond diffuse necking up to localized rupture, and is therefore of limited use for quantifying the deformation and failure behavior of spot-weld materials at large strains.

The small dimensions of the miniature tensile bars required a new approach to tensile testing that differed from the conventional approach. The new approach would have to reliably capture both small and large strains in the miniature tensile bars, and provide true stress-strain relations beyond diffuse necking (which is especially important for materials that exhibit low strain-hardening rates and, thus, small onset strains of diffuse necking). The newly developed digital image correlation (DIC) technique was found to be ideal for this application. Recently, this technique has been used to measure whole-field surface displacements and strains at various length scales, ranging from individual grains to large

deformation bands in aluminum alloys (*i.e.*, the so-called Portevin–Le Chatetiler effect), and crack nucleation and growth in NiTi shape memory alloys.[18–25] In this investigation, plastic deformation up to ductile rupture of miniature tensile bars machined from different metallurgical zones of dual-phase steel resistance spot welds is quantified with the new experimental methodology based on high-resolution, whole-field deformation mapping by DIC. Quasi-static, uniaxial tensile, true stress-strain curves were obtained up to localized necking and rupture, using the new experimental methodology. The influence of the different weld-joint microstructures on the tensile test results was also explored, in order to gain fundamental knowledge of their relation with the deformation and fracture behavior of resistance spot welds.

The organization of this article is as follows. In Section II, the experimental procedure is detailed, which includes the spot welding process used to generate the test materials, the material microstructural characterization, the nanoindentation tests, the uniaxial tensile tests, and the digital image correlation (DIC) analysis is detailed. In Section III, the tensile testing results are presented and the effects of various material microstructures on their plastic deformation and failure behavior are discussed in detail. In Section IV, the results of this work are summarized.

II. EXPERIMENTAL PROCEDURE

A. *Material Preparation*

Cold-rolled, galvanized, dual-phase steel sheets, 2.0 mm in thickness and supplied by National Steel (Mishawaka, IN), were used in this study. The dual-phase microstructure in the steel selected for this investigation resulted from an appropriate combination of heat treatment and chemical composition (summarized in Table I). As in other dual-phase steels, manganese, chromium, and carbon were the main alloying elements, and their concentrations were comparable to other commercial dual-phase steels. The minimum YS and ultimate tensile strength (UTS) were 340 and 590 MPa, respectively. The resistance spot welds were fabricated using direct-current and single-pulse schedules on two identical overlapping dual-phase steel coupons, each 127 mm long and 38 mm wide (Figure 1(a)). The welding current and the welding hold time were set in the vicinity of 10 kA and 20 cycles (*i.e.*, 1/3 second), respectively. This combination of welding process parameters was found to consistently generate welds 6 to 7 mm in diameter. Increasing the welding hold time to 30 cycles (1/2 second) produced no significant changes in the weld microstructures. Due to concerns about defects in the weld microstructure (*e.g.*, voids, cracks, and zinc contamination), welding was also conducted with additional currents of 9.0, 9.5, 10.5, and 11.0 kA, which were used as a precautionary measure to reduce the contribution from such potential defects. The heat-affected zone samples were prepared following a similar procedure, but using a single coupon rather than a

Table I. Chemical Composition of the Dual-Phase Steel in Weight Percent

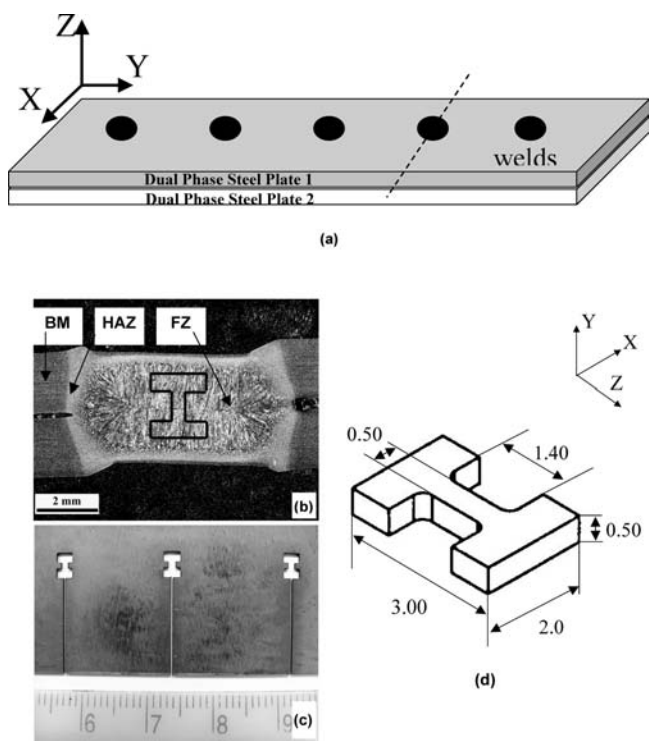| C	Mn	Cr	Mo	Ni	Ti	V	Al	Si	P	S	B	N	O
0.11	1.50	0.27	<0.005	0.02	<0.005	0.06	0.06	0.1	0.02	<0.003	<0.001	0.0065	0.0028

Fig. 1—Miniature tensile bars, specifically (*a*) the two overlapping dual-phase steel coupons (127 mm long and 38 mm wide) with five spot welds, (*b*) a cross-section showing both an outline how and where the spot weld tensile bars were cut and the three material zones (BM: base metal; HAZ: heat-affected zone; and FZ: fusion zone), (*c*) the cutouts of the heat-affected zone and base metal tensile bars with a comparison using a millimeter scale, and (*d*) a three-dimensional view, with dimensions in mm. The dashed line in (a) indicates where the cross-section plane in (b) was cut for spot-weld tensile bars.

two-coupon stack. A shorter time (less than ten cycles, or 1/6 second) was used to generate less heat than during normal welding, while the current was kept constant at 10 kA. A peak temperature lower than the alloy solidus point and the subsequent rapid cooling ($>10^3$ °C/s) guaranteed the formation of microstructures comparable to heat-affected zones in real weld joints. Both a metallographic examination and a nanoindentation test were used to verify the microstructures of the simulated heat-affected zone materials.

Miniature tensile bars with a square cross section were cut in the resistance spot welds, heat-affected zone, and base metal samples using a wire electrical discharge machine (EDM). The orientation and location of the tensile bars cut from the fusion zone, the simulated heat-affected zone, and the base metal are shown in Figures 1(b) and (c), respectively. The shape, dimensions (in mm), and orientation for bars cut from the fusion zone are given in Figure 1(d). In the fusion zone tensile bars, the cross-sectional plane at the center of the gage section was selected to be the joined interface of the two steel sheets, as shown in Figure 1(b). The three material zones (BM: base metal; HAZ: heat-affected zone; and FZ: fusion zone) are also indicated in Figure 1(b). Note that the tensile bars were cut carefully in a plane that contained the center axis of each spot weld. Since machining-induced defects are of concern in wire electrical discharge processes, the feed rate was intentionally fixed at 4.8 mm/min. This was judged to be slow enough so as to preclude defect formation during miniature

tensile bar preparation. Miniature tensile bars were also cut *via* an EDM from the as-received dual-phase steel sheets, as the reference (base) material. Additional tensile bars with a gage section measuring 20 mm long, 5 mm wide, and 2 mm thick were also cut from the 2-mm-thick base material, so that any possible effects of geometry, dimensions, and the EDM machining of tensile test samples on the deformation and failure behavior of the base materials could be examined. In this study, these larger tensile bars will be referred as compact tensile bars, as they were about one-third the length and width of the standard ASMT E8 tensile coupons for sheet metals.

B. *Microstructure Characterization and Nanoindentation Testing*

Many of the welds were cross-sectioned for microstructural and defect analyses. Following standard metallographic preparation and etching with Nital, weld cross sections were examined using optical, electron, and atomic force microscopy. Wavelength spectroscopy with a microprobe analyzer was also used to further detail the weld solidification microstructure, particularly by mapping alloying element concentrations throughout the fusion zone. Load-indentation curves from indents at spatial increments of 20 μm across the base material, heat-affected zone, and fusion zone were measured using a Berkovich tip. The indents were limited in depth to 1000 nm (*i.e.*, not load controlled). The hardness and elastic modulus were computed from the slope of the unloading curve *via* the Oliver–Pharr method (assuming a Poisson ratio of 0.3).[15] Fractured tensile bars were examined using a scanning electron microscope (SEM) to determine both fracture mechanisms and the potential presence of subsurface defects. The cross-sectional area of the projected fracture surface of each test bar was measured based on secondary electron images and it was used for estimating the true strain at the final failure of each test bar. Energy-dispersive spectroscopy was applied to measure chemical compositions at fracture surfaces. This technique was preferred over wavelength spectroscopy, since the rough topography of the fracture surface rendered application of the latter problematic; this was true even though the wavelength spectroscopy technique is ten times more precise.

C. *Tensile Testing Procedure*

To test the miniature tensile bars, stainless steel grippers were fabricated for a small desktop tensile testing apparatus with a 50-mm total travel and 4400-N load capacity. The grippers, which are depicted in Figure 2(a), were adjusted to align both horizontally and vertically with the bar ends. The tensile bars were placed into an open slot located between the grippers, as shown in Figures 2(b) and (c), and then strained to fracture (Figure 2(d)). All tensile tests were conducted at a constant crosshead speed of 0.2 μm/s (corresponding to a nearly constant strain rate of 2×10^{-4} 1/s), using a stepping motor. The larger compact tensile bars of the base material were tested at comparable nominal strain rates in an MTS-810 hydraulic universal materials testing machine.

Prior to tensile testing, the surfaces of the tensile bars were examined for pre-existing cracks and machining irregularities: none was noted on any of the tensile bars. One surface from the gage section of each tensile bar was then decorated with a pattern of random contrast features, to facilitate the
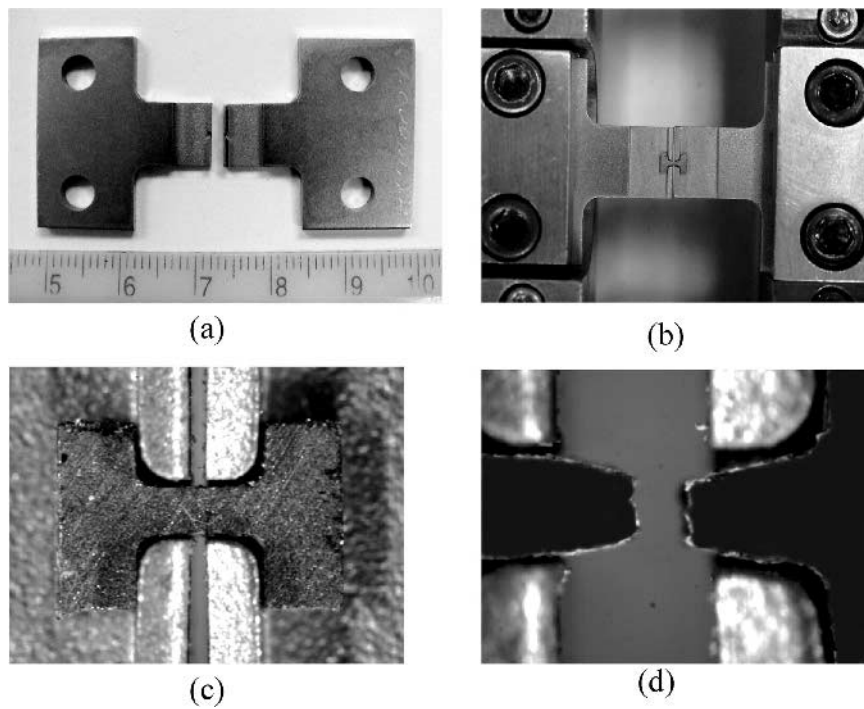
Fig. 2—Images of (a) the grippers relative to a millimeter scale, (b) the tensile bar placed between grippers prior to tensile testing, (c) the tensile bar of (b) at a higher magnification, and (d) the tensile bar when it fractured.

DIC process. For the miniature tensile bars extracted from the weld fusion zones (Figure 1(b)), the heat-affected zones, and base metals (Figure 1(c)), a thin (i.e., 0.02- to 0.05-mm) coating of white spray paint was applied, directly followed by a sprinkling of fine black laser toner powder. Following the decoration process, each tensile bar was baked at 95 °C for 30 minutes, to enhance adhesion of the laser toner particles to the steel surface. The baking step did not significantly affect the strength of the tensile bars. The surfaces of the larger base metal tensile bars were decorated with fine speckles of black spray paint. All tensile bars were tested as machined, without further grinding and polishing of their surfaces.

After decorating the tensile bar surfaces with paint speckles or laser toner powder, digital images were captured during tensile testing, using a black-and-white CCD camera equipped with a zoom lens and a frame grabber. The time history was logged by tracking the stepping number of the stepping motor and associating the recorded axial load and displacement of the tensile testing apparatus with a given stepping number. All data were recorded at a sampling rate of 8 Hz. A series of grayscale 640×480-pixel digital images of the entire surface of each bar was recorded during each test, with a spatial resolution of 3.3 μm/pixel and at intervals of 15 to 30 seconds. A total of 27 tensile test samples (13 miniature tensile bars fabricated from the weld fusion zones, 5 miniature tensile bars made from the heat-affected zone samples, and 3 miniature tensile bars and 6 larger compact tensile bars cut from the base material) were quasi-statically tested up to complete fracture.

D. DIC Data Analysis

Displacement fields were extracted from the comparisons between the contrast features in pairs of digital images

acquired before and after the application of a strain increment in a tensile testing.[18] The region of interest in the digital images was first defined with a set of virtual grid points (similar to nodes in a finite element mesh) positioned at the center of user-specified subset arrays (or small area elements) within each image. An example of a 39×43 digital grid superimposed on digital images of a tensile bar surface before and after a deformation increment is shown in Figures 3(a) and (b), respectively.[20,25] Six affine-mapping parameters (detailed in Reference 18) were then computed at each grid point to account for the in-plane homogeneous deformation and rigid body motion of the associated image subset. Additional post-processing filtering and smoothing was then used to compute the translation, rotation, extension, and shear of each subset. The in-plane true strain components, ε_1, ε_2, and ε_{12} at each load step, were finally computed from a consecutive set of digital images for the entire tensile test. Square grids with a spacing of 5 pixels (16.5 μm) and a subset of 40×40 pixels (0.132 mm $\times$ 0.132 mm) were used in this study. For a macroscopically homogeneous field, errors in the local in-plane displacements, rigid body rotation, and strain measurements were estimated to be 0.02 pixels (0.48 μm), 0.02 deg, and 400 μstrains, respectively.[19]

The average axial strain was entered into the following equation based upon force equilibrium along the tensile loading direction, for computing the average axial true stress in a tensile bar:

$$\bar{\sigma}_1 = \frac{Fe^{\bar{\varepsilon}_1}}{WT} \qquad [1]$$

where F is the currently applied axial load, W and T are the initial width and thickness of the tensile bar, respectively, $\bar{\varepsilon}_1$ is the average axial true strain measured by the DIC
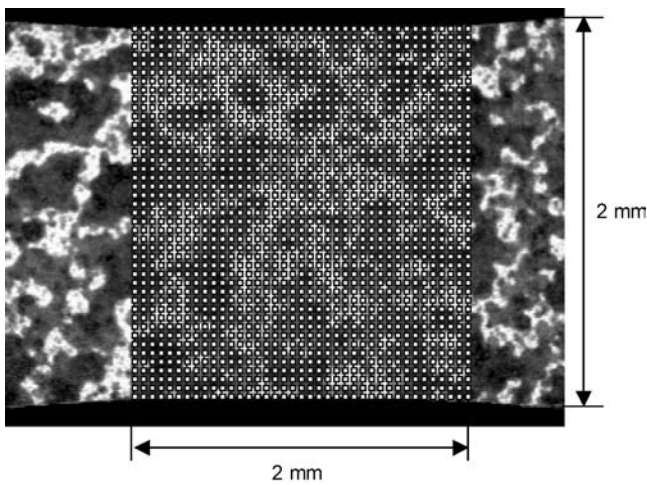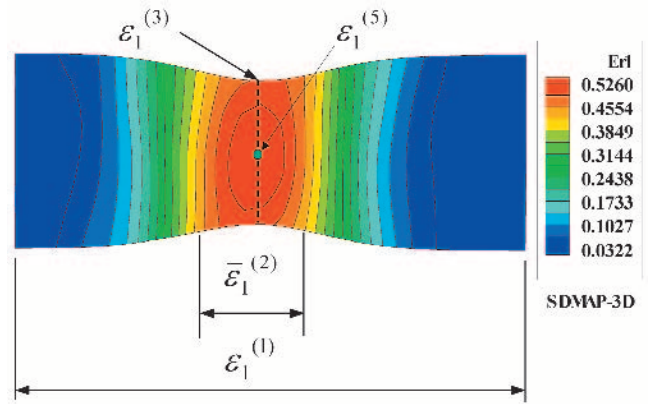
(a) Before deformation
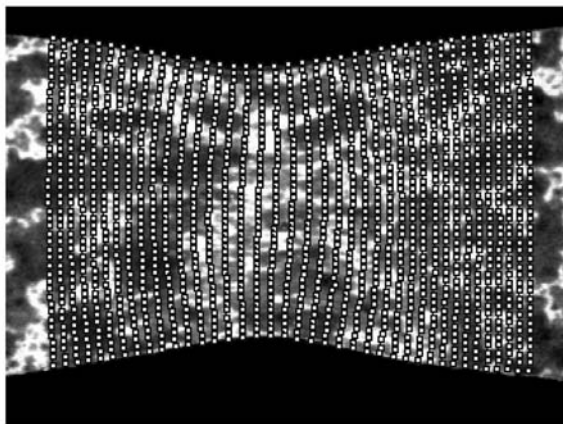
(b) After a deformation increment

Fig. 3—Virtual grid patterns (39 × 43) superimposed onto a tensile bar surface (*a*) before and (*b*) after deformation increments.
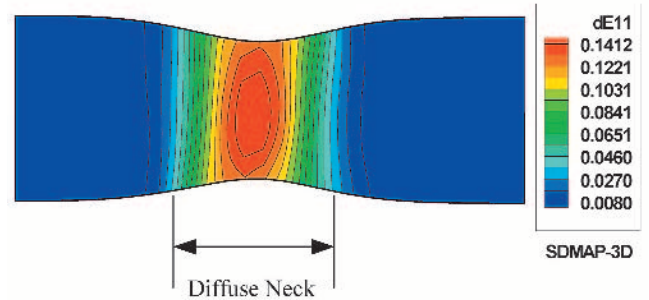

(a) a cumulative axial strain map

(b) an incremental axial strain map

Fig. 4—(*a*) A cumulative strain Er1 map of a tensile bar and definitions of various average true axial strains (see Eqs. [2] through [5] for details) and (*b*) an incremental axial strain dE11 map obtained *via* the correlation of a pair of images at two adjacent load steps. The spatial extent of the diffuse neck at the current load step can be estimated based on the plastically deforming region shown in the incremental strain map.

technique, and $\bar{\sigma}_1$ is the average axial true stress. This equation applies as long as the volume constancy of plastic deformation is guaranteed and as long as the stress state is fairly unidirectional. Previous work[20,25] has revealed that the stress-strain state in the neck region in a thin sheet deviates only slightly from that of uniaxial tension, despite increasingly heterogeneous strain distributions. Equation [1] is therefore a reasonable approximation of the uniaxial tensile stress-strain curve beyond the onset of diffuse necking and up to considerably larger strains, if a proper average axial strain measure is used.

In Eq. [1], the definition of the average axial true strain, $\bar{\varepsilon}_1$, is somewhat flexible with the DIC technique. Four definitions of the average axial true strain measures were employed in this study, as shown in Figures 4(a) and (b) (these are typical cumulative and incremental axial strain maps, respectively, just after the onset of diffuse necking in a tensile test). The corresponding mathematical definitions of the average strain measures are as follows:

$$\bar{\varepsilon}_1^{(1)} = \frac{1}{MN} \sum_{j=1}^{N} \sum_{i=1}^{M} \varepsilon_1(i, j) \qquad [2]$$

where $\bar{\varepsilon}_1^{(1)}$ is the axial strain averaged over the entire gage section (following the conventional tensile test methodology), M and N are the total numbers of grid points along the gage length and width directions, respectively, and $\varepsilon_1(i, j)$ is the local axial strain at each grid point (i, j) obtained *via* DIC;

$$\bar{\varepsilon}_1^{(2)} = \frac{1}{M_n N} \sum_{j=1}^{N} \sum_{i=M_1}^{M_1+M_n} \varepsilon_1(i, j) \qquad [3]$$

where $\bar{\varepsilon}_1^{(2)}$ is the axial strain averaged over the entire neck region (this is the lower-bound estimate of average strain in the diffuse neck), M_1 and M_n are the starting and total number of grid points, respectively, along the gage length direction of the neck region (Figure (4a));

$$\bar{\varepsilon}_1^{(3)} = \frac{1}{N} \sum_{j=1}^{N} \varepsilon_1(M_0, j) \qquad [4]$$

where $\bar{\varepsilon}_1^{(3)}$ is the axial strain averaged along the bar cross section with the smallest width (*i.e.*, the neck center line at $i = M_0$, as in Figure (4a));

$$\bar{\varepsilon}_1^{(5)} = \varepsilon_1(M_0, N_0) = \max_{j=1,N} [\varepsilon_1(M_0, j)] \qquad [5]$$

where $\bar{\varepsilon}_1^{(5)}$ is the maximum axial strain at the center of a diffuse neck corresponding to the grid point (M_0, N_0). This definition of axial strain provides the upper-bound estimate of the measurable average strain in the diffuse neck. Since the entire gage section was used to compute $\bar{\varepsilon}_1^{(1)}$, local strain heterogeneities and gradients were averaged out over the gage section. Alternatively, the strain fields selected for computing $\bar{\varepsilon}_1^{(2)}$, $\bar{\varepsilon}_1^{(3)}$, and $\bar{\varepsilon}_1^{(5)}$ were measured over the entire neck region, or a selected part of the neck region; hence, local strain heterogeneities were more accurately quantified. Both analytical and numerical analyses have shown that the average axial true strains $\bar{\varepsilon}_1^{(2)}$ and $\bar{\varepsilon}_1^{(3)}$ as defined by Eqs. [3] and [4], respectively, are the most accurate estimates[20,25] of uniaxial true strain and true stress (via Eq. [1]), beyond diffuse necking in various tensile bar geometries. The definitions $\bar{\varepsilon}_1^{(1)}$ and $\bar{\varepsilon}_1^{(5)}$ provide uniaxial true stress-strain curves that bound the actual uniaxial true stress-strain curve, irrespective of tensile bar geometry.

III. EXPERIMENTAL RESULTS AND DISCUSSION

A. Microstructural Characterization

Figures 5(a) through (f) show both the optical macrographs of a typical resistance spot weld and the atomic force microscopy images (all with a full field of view, 25×25 μm^2

in size) of the internal microconstituents observed at dual-phase steel weld joints. The low-magnification pictures in Figures 5(a) and (b) show complementary views of one-half of a spot weld and reveal the base metal, heat-affected zone, and fusion zone (which are labeled, respectively, BM, HAZ, and FZ). Figure 5(a) shows the microstructure viewed from the top of the weld, and Figure 5(b) shows the microstructure along a slice through the thickness of the welded steel sheets. Based upon the different degrees of etching, the heat-affected zone appeared as a gradient of microstructures, all surrounding a comparatively coarser grain structure in the fusion zone. Note that the width of the heat-affected zone was of the order of 0.5 to 0.7 mm. In contrast, the fusion zone was approximately ten times larger, reaching a diameter of slightly over 7 mm. Unlike the heat-affected zone and the base materials, the weld fusion zone microstructure exhibited a distinct directionality, as best seen in Figure 5(b). An array of columnar grains, extending from the heat-affected/fusion zone elliptic boundary all across the fusion zone, can be observed. Such directionality in the fusion zone microstructure raised the possibility that resistance spot welds might deform anisotropically.

The various microstructures of the different regions in Figures 5(a) and (b) (due to variations in thermal cycles experienced by the material) are magnified in the atomic force microscopy images in Figures 5(c) through (f), moving left to right across the zones in Figure 5(b). Figure 5(c) shows the dual-phase steel microstructure in the base material,
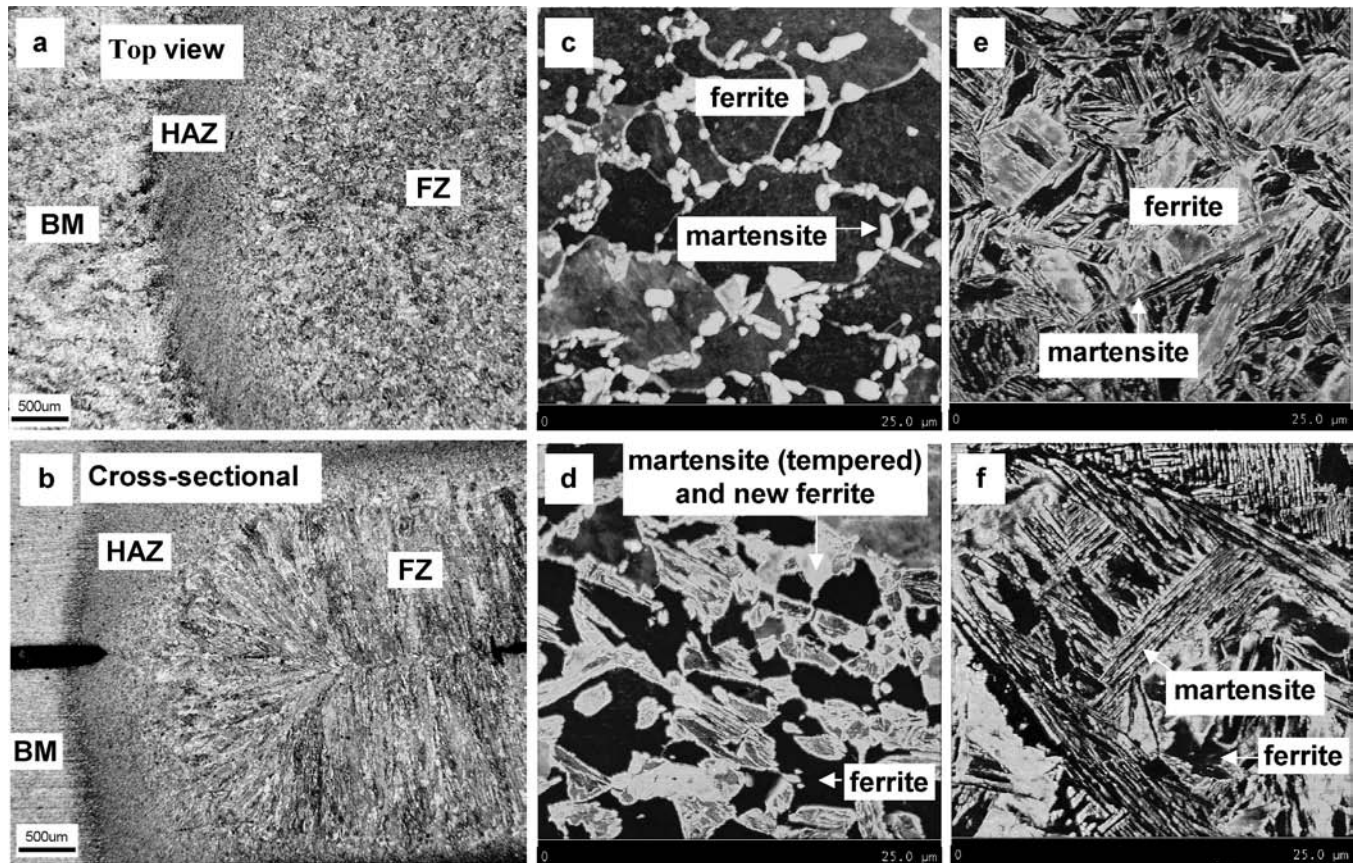

Fig. 5—A set of micrographs depicting the typical microstructures seen in resistance spot welds of dual-phase steels. In these micrographs, (a) and (b) show complementary optical micrographs of one-half of a spot weld and (c) through (f) are atomic force microscopy amplitude images (all with a field of view of 25×25 μm^2) that reveal the morphology of the internal microstructures (after etching) for (c) the base material, (d) and (e) the heat-affected zone, and (f) the center of the fusion zone.

which consists of fine polygonal ferrite gains (dark phase) decorated with islands of martensite (bright phase).[1,2,3] Area counts showed that this dual-phase microstructure was comprised of approximately 20 pct martensite (interchangeably by volume or weight). Figure 5(d) shows a region of the heat-affected zone close to the base material, where the original martensite began to decompose into austenite before being retransformed upon rapid cooling into a new martensite and a new ferrite.[2,3] Figure 5(e) captures an entirely new microstructure for the part of the heat-affected zone region in closer proximity to the weld fusion zone. A polygonal grain structure, formed after ferrite and martensite fully transformed into austenite, is still visible. The fine needle-like phase seen in Figure 5(e) is a typical martensitic morphology. In reference to Figure 5(c), the coarser phase along the grain boundaries may be ferrite. The microstructure of Figure 5(f), which is near the center of the fusion zone, resembles that

of Figure 5(e). The martensite needles appear to have been less impeded by grain boundaries, which could explain their greater lengths.

Figure 6(a) shows a high-magnification electron backscattered image of the central part of the weld fusion zone, with voids along interdendritic boundaries outlined by yellow boxes superimposed on the image. Figures 6(b) through (d) show X-ray dot maps of the weld fusion zone in Figure 6(a), with the bright colors denoting rich concentrations of manganese, oxygen, and silicon, respectively. Figure 6(b) clearly demonstrates that manganese is heterogeneously distributed within the new microstructure of the weld fusion zone. The richest manganese regions seen in Figure 6(b) reveal the dendritic substructure of the weld, as if the microstructure were directly observed at high temperature when solidification ended. Figures 6(c) and (d) show oxygen and silicon, respectively, deeply imbedded within the microstructure.
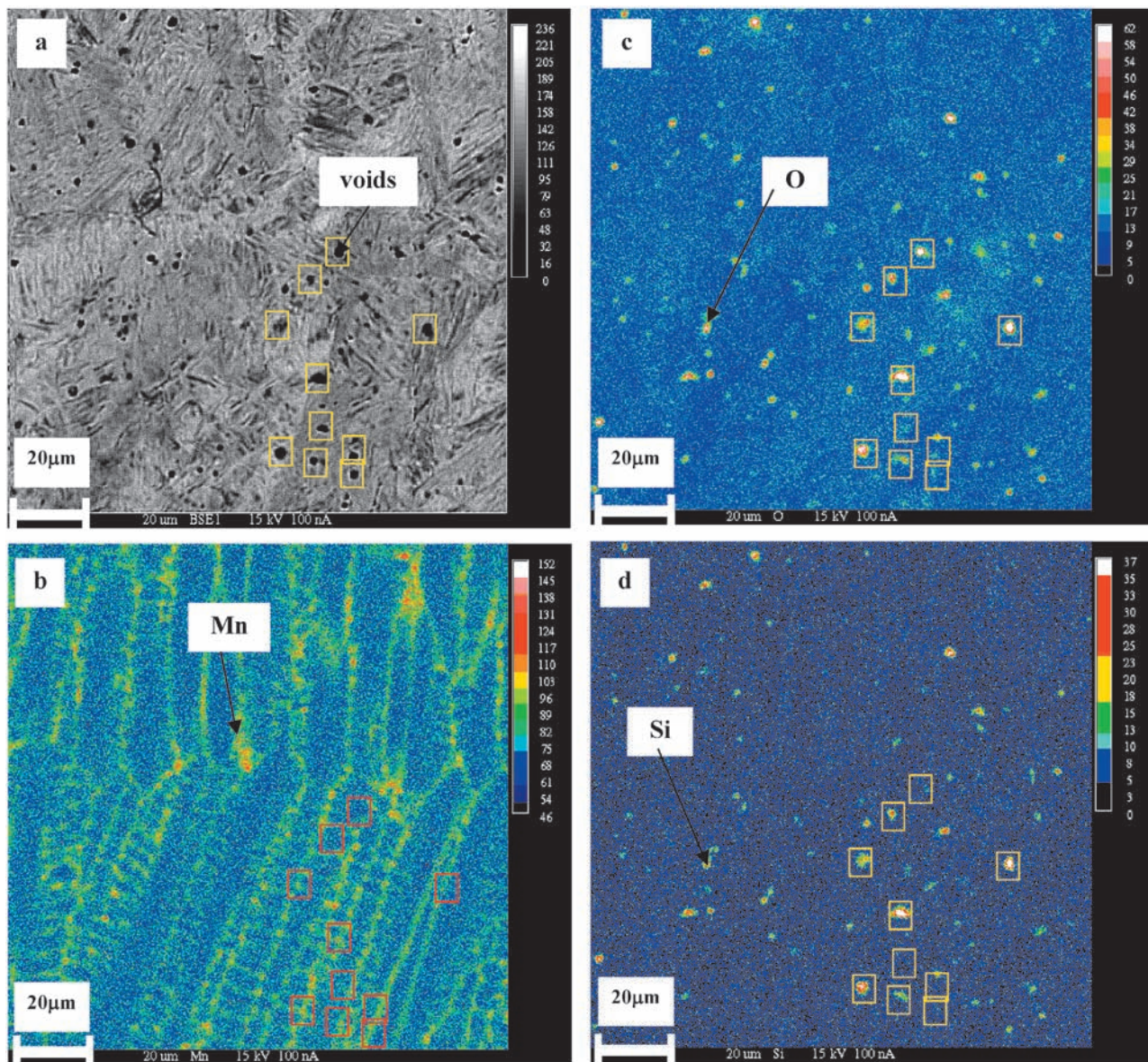

Fig. 6—The as-solidified weld microstructure, specifically (*a*) a high-magnification electron backscattered image of the central part of the weld fusion zone, with voids along interdendritic boundaries outlined by yellow boxes superimposed on the image. (*b*) through (*d*) X-ray dot maps of the weld fusion zone in (a), with the bright colors denoting rich concentrations of manganese, oxygen, and silicon, respectively.

Despite large uncertainty, analyses by energy-dispersive spectroscopy proved that silicon-to-oxygen atomic ratios were less than 0.4, strongly suggesting that silicon and oxygen were combined in the form of silica (SiO_2). Confirmation can be seen in the various images of Figure 6, where the greatest counts of oxygen (Figure 6(c)) and silicon (Figure 6(d)) X-rays appear to superimpose perfectly. Most important, the counts of oxygen and silicon coincided with the dark spots shown in the yellow boxes in Figure 6(a), which were all located along the dendritic boundaries revealed by the manganese map in Figure 6(b). Knowing that oxygen and silicon were introduced during final polishing with colloidal silica, it may be concluded that the dark spots seen on Figure 6(a) are microvoids that trapped silica during polishing. In all likelihood, these voids resulted from solidification shrinkage, an unavoidable consequence of the thermal expansion differences between the solid and liquid phases of iron.

Figure 7 shows results from nanoindentation measurements across the base material, heat-affected zone, and fusion zone. The reported hardness numbers (in GPa) were derived using the Oliver–Pharr method,[15] where an asymmetric pyramidal diamond indenter was used. As shown in Figure 7, the new microstructures created by rapid solidification produced a significant strengthening (which was found to be independent of the applied welding current). On average, the hardness of the weld fusion zone was 3.93 GPa, and was about 75 pct greater than that in the base material (2.37 GPa). Hardness in the heat-affected zone fell within the various metallurgical zones; significant variations in hardness were recorded as indents were produced in the various phases illustrated in Figures 5(c) through (f). The large variations of hardness within the base material (over 1.0 GPa) and the weld fusion zone (as high as 2.0 GPa) were attributed to the two major phases, i.e., ferrite and martensite. The considerably finer microstructure of the rapidly solidified weld fusion zone (Figure 5(f)), as well as anticipated variations in chemical composition, clearly produced harder microstructures and greater variations in hardness. More martensite content and

heterogeneities (as expected from a solidified microstructure) can be seen in the fusion zone than in the base material (Figures 6(b) and 1(b)). The part of the heat-affected zone closer to the fusion zone is entirely composed of martensite, and its hardness (or tensile properties) is typically highest. The heat-affected zone microstructure is comparatively free of defects and, of course, is more homogeneous, since the structure has remained granular (only solid-solid phase transformation occurs in the heat-affected zone).

In dual-phase steels, as in most welded alloys, the properties of the heat-affected zone are intermediate to those of the base material and the fusion zone, as can be seen in Figure 6. The heat-affected zone is typically very narrow, i.e., about 0.5 mm wide, compared to several millimeters for the fusion zone. Therefore, even the miniature tensile bars (Figure 1(b)) were not sufficiently small to easily capture solely the heat-affected zone microstructures of the spot welds. As an alternate solution, larger samples, using thermal cycles that are comparable to those experienced by the heat-affected zone (i.e., a peak temperature lower than the alloy solidus point and a very rapid cooling ($>10^3$ °C/s)) were used. Consequently, the simulated heat-affected zone materials were also produced using the resistance welding process, but using only one sheet rather than two and a shorter hold time (while the current was kept constant, as shown in Table III). Miniature coupons were cut in the plane of each sheet at different orientations. The sample orientation was found to play no role in the measured tensile properties of the simulated heat-affected zone samples. Different welding process parameters could have been selected, but this would not have noticeably changed the results. Indeed, from published work, the heat-affected zone hardness in steels is affected by process parameters by less than 10 pct,[7,10] providing that the weld is cycled once (several thermal or weld cycles are often employed to temper the microstructure). A single-thermal cycle or current pulse was employed in this study to produce all of the simulated heat-affected zone materials. To ascertain whether the heat-affected zone samples truly exhibited the similar properties of heat-affected zone material from spot welds, several simulated heat-affected zone samples were prepared for metallographic examination. Microstructures similar to those shown in Figures 5(d) and (e) were seen. While it was found difficult to control the process parameters in order to produce these heat-affected zone microstructures with consistency, the procedure described above allowed us to generate microstructures with a sufficiently wide range, as observed in actual spot-welded joints (Figures 5(a) through (e)).

B. Summary of Tensile Testing Results

Table II summarizes some of the major results from tensile testing of 5 base material tensile bars, 5 heat-affected zone tensile bars, and 13 fusion zone tensile bars. For reference purposes, the samples were numbered, as listed in the second column of Table II. Only two of them (GMT #33 and #34, each made of the base material) made of the base material were compact tensile bars with a rectangular cross section. All of the other 21 tensile bars listed in Table II were the miniature type with a square cross section, as shown in Figure 1(d). The YS (i.e., the stress corresponding to a 0.2 pct offset in total strain) and the UTS (i.e., the strength
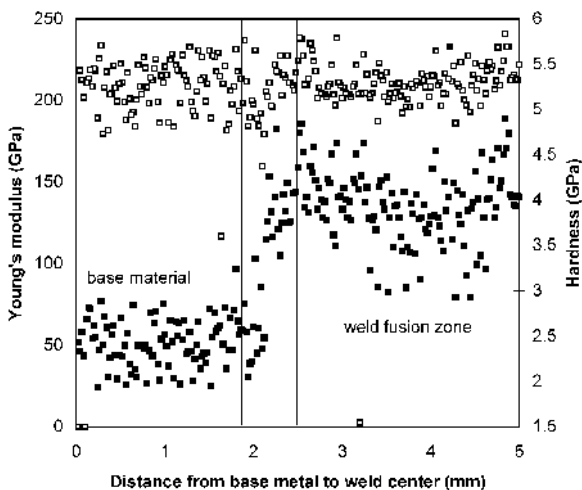

Fig. 7—Hardness distribution (solid squares) from nanoindentation across one-half of a resistance spot weld cross section, starting in the unaffected base material and finishing at the weld center. The Young's modulus (open squares) of the material is also shown. The average hardness values for the base material and the weld fusion zone are 2.37 and 3.93 GPa, respectively.

Table II. Summary of Tensile Testing Results for the Three Weld Regions

Material Type	Sample Number	YS (MPa)	Eng. UTS/True UTS (MPa)	Eng. Strain at UTS	True Stress at 8 Pct (MPa)	True Strain at Failure[1]	True Stress at Failure (MPa)[2]
Base material	GMT #33[3]	350	597/728	0.220	604	1.04	1342
	GMT #34[3]	365	600/730	0.220	612	1.14	1418
	GMT #92	320	556/697	0.225	564	1.26	1310
	GMT #93	298	552/685	0.215	540	1.20	1290
	GMT #94	336	571/705	0.210	551	1.22	1303
	Average 1[4]	358	599/729	0.220	608	1.09	1380
	Average 2[5]	318	560/696	0.216	552	1.23	1301
Simulated heat-affected zone	GMT #76	1361	1422/1488	0.046	1518	0.86	1820
	GMT #77	548	784/918	0.171	835	1.12	1555
	GMT #79	443	579/740	0.278	587	1.43	1492
	GMT #81	428	589/731	0.241	603	1.69	1614
	GMT #83	1185	1505/1595	0.060	1633	0.81	2191
	Average 1[6]	473	651/796	0.230	675	1.41	1554
	Average 2[7]	1273	1464/1542	0.053	1576	0.84	2006
Weld fusion zone	GMT #21	988	1201/1261	0.050	1301	0.95	2058
	GMT #23	1058	1202/1251	0.040	1299	0.48	1432
	GMT #24	1050	1224/1291	0.055	1325	1.12	2079
	GMT #25	1016	1219/1284	0.053	1315	1.30	2062
	GMT #26[8]	860	1121/1201	0.050	—	—	—
	GMT #27	880	1098/1131	0.030	(1161)	(0.26)	(840)
	GMT #28	965	1266/1347	0.064	1385	1.03	2073
	GMT #29	867	1180/1255	0.063	1288	0.88	1447
	GMT #30	835	1204/1289	0.071	1306	0.87	1732
	GMT #31	887	1248/1364	0.093	1352	1.14	2344
	GMT #78	831	952/1004	0.053	(1036)	(0.25)	(654)
	GMT #80	1035	1429/1522	0.065	1546	1.04	2139
	GMT #82	1038	1268/1315	0.037	(1284)	(0.40)	(1225)
	Average[9]	967	1241/1318	0.062	1346	0.98	1930

[1]Estimated from the area of fracture surfaces measured by SEM.
[2]Estimated from the load at fracture and the fracture area based on SEM measurements.
[3]Compact tensile bars used (with a gage section of $20 \times 5 \times 2$ mm^3). All others were miniature bars (with a gage section of $1.4 \times 0.5 \times 0.5$ mm^3), as shown in Figure 1(d).
[4]Averaging results of the two tests, for GMT #33 and #34.
[5]Averaging results of the three tests, for GMT #92, #93, and #94.
[6]Averaging results of the three tests, for GMT #77, #79, and #81.
[7]Averaging results of the two tests, for GMT #76 and #83.
[8]Edge cracking was observed for test bar GMT #26, but it was not stretched to complete rupture.
[9]Averaging results of the nine tests, for GMT #21, #23, #24, #25, #28, #29, #30, #31, and #80.

at the maximum load) are given in the third and fourth columns, respectively. As shown in Table II, definitions based upon both engineering and true strains were considered. The engineering strain at the UTS is also reported in the fifth column. However, since engineering and true strains are comparable at such small plastic strains, corresponding true strains were not included in Table II. The true flow stress at the 8 pct true plastic strain, which is reported in the sixth column, was included in Table II to compare with hardness, as these two quantities appear to be quite well correlated by a factor of about 3 for ductile metals.[14] As shown in Figure 7, the average hardness numbers for both the base material and weld fusion zones were 2.37 and 3.93 GPa, respectively. These are 3.9 to 4.3 and 2.9 times the (average) true flow stresses at the 8 pct plastic strain of the base materials and fusion zone materials, respectively.

Each of the stress quantities in Table II was computed *via* Eq. [1], using the average axial strain defined in Eq. [4]. The true strain and true stress values at failure, which are listed in the seventh and eighth columns, respectively, are only rough estimates of these quantities, since they are derived from measurements of projected areas, based on secondary electron images of fracture surfaces. Uncertainties on the order of 15 to 25 pct remain in both the load at the fracture point and the corresponding fracture area. Note that the quantities found in parentheses in Table II are associated with tensile bars that failed prematurely. Because recorded axial load displacements and stress-strain relationships were substantially different when cracking occurred off center rather than through the central part of the tensile bars (normal symmetric diffuse necking behavior), the results to be discussed in the following sections have been categorized accordingly.

In Table II, the results for the simulated heat-affected zones were indicative of two types of microstructures categorized as "soft" (GMT #77, #79, and #81) and "hard" (GMT #76 and #83). For the soft heat-affected zone, yield strengths were between 428 and 548 MPa, while the corresponding values for the hard heat-affected zones exceeded 1100 MPa (1361 and 1185 MPa, respectively). Such discrepant results suggest that the heat-treatment by the shorter pulsed spot welding used to produce the simulated heat-affected zones was somewhat

Table III. Summary of Failure Type and Fracture Surface Characteristics of Miniature Tensile Bars

Sample	Sample Type	Welding Current and Hold Time	Failure Type	Fracture Surface Type
21	fusion zone	9.0 kA, 20 cycles	necking and rupture*	coarse dimples
23	fusion zone	9.5 kA, 20 cycles	premature cracking at edges**	cracks and voids
24	fusion zone	10.0 kA, 20 cycles	necking and rupture*	coarse dimples
25	fusion zone	10.5 kA, 20 cycles	necking and rupture*	coarse dimples
26	fusion zone	9.0 kA, 20 cycles	premature cracking at edges**	did not load to rupture
27	fusion zone	9.0 kA, 20 cycles	premature cracking at edges**	cracks and voids
28	fusion zone	9.5 kA, 20 cycles	necking and rupture*	cone-shaped surface
29	fusion zone	10.0 kA, 20 cycles	necking and rupture*	coarse dimples
30	fusion zone	10.5 kA, 20 cycles	necking and rupture**	coarse dimples
31	fusion zone	9.0 kA, 20 cycles	necking and rupture*	coarse dimples
76	heat-affected	9.0 kA, 6 cycles	necking and rupture*	coarse dimples
77	heat-affected	9.0 kA, 5 cycles	necking and rupture*	fine voids and dimples
78	fusion zone	9.0 kA, 20 cycles	premature cracking at edges**	extensive melt metal
79	heat-affected	9.0 kA, 5 cycles	necking and rupture**	fine voids and dimples
80	fusion zone	9.0 kA, 20 cycles	necking and rupture*	coarse dimples
81	heat-affected	9.0 kA, 6 cycles	necking and rupture**	fine void and dimples
82	fusion zone	9.0 kA, 20 cycles	premature cracking at edges**	extensive melt metal
83	heat-affected	9.0 kA, 6 cycles	necking and rupture*	coarse dimples
92	base metal	—	necking and rupture*	fine voids and dimples
93	base metal	—	necking and rupture*	fine voids and dimples
94	base metal	—	necking and rupture*	fine voids and dimples

*Ductile failure within the neck region, usually initiating at the point of maximum strain.
**Defect-induced cracking in the gage section.

variable. Recall that the simulated heat-affected zones, exactly like the heat-affected zones of real weld joints, were comparably heterogeneous, as is depicted in Figures 5 and 7 for an actual spot weld. This characteristic of the simulated heat-affected zones is difficult to change unless a totally new heat-treating procedure is developed. Despite the obvious differences, the results observed in the simulated heat-affected zones were worth comparing to those of the fusion zones and base materials.

Within the inherent uncertainties of the true stress and true strain at fracture, the base materials and the simulated soft heat-affected zone have comparable fracture behavior when miniature tensile bars are used. On the other hand, the failure of the simulated hard heat-affected zone is similar to that of a good fusion weld zone. For the base material, the average axial strain based on the fracture surface area of the miniature tensile bars with a square cross section (a thickness-to-width ratio of 1:1) was found to be higher than that of the compact tensile bars with a rectangular cross section (a thickness-to-width ratio of 1:2.5). The additional ductility in the square cross-section tensile bars can be attributed to enhanced stress triaxiality inside a diffuse neck, so localized necking was delayed. Nonetheless, the level of ductility measured in the tested specimens is remarkable. Tensile strains at rupture were repeatedly near and above 100 pct (*i.e.*, a true strain of one).

Table III complements Table II by providing further information such as welding parameters (current and hold time), type of failure, and major characteristics of fracture surfaces for both the heat-affected zones and the fusion zones. As indicated in Table III, many of the tensile bars fractured in the symmetric neck region at or near the center of the gage section. This type of fracture was observed in all types of microstructures. However, an uncharacteristic edge cracking that led to premature fracture was also encountered, but, surprisingly enough, only in the weld fusion zones. Since this type of fracture was unique to weld fusion zones, the possibility that subsurface defects were introduced during welding was of concern. The edge cracking in the weld fusion zones will be revisited following a careful examination of those zones that exhibited normal ductile failure.

C. *Normal Plastic Response (Symmetric Diffuse Necking and Ductile Rupture)*

1. *Base material (dual-phase steel)*
Figure 8(a) shows a set of five curves generated from one tensile testing experiment on GMT #34 (Table II), using a compact tensile bar with a rectangular cross section. The four different true stress-strain curves, labeled 1, 2, 3, and 5, were obtained based on the four different average axial strains defined by Eqs. [2] through [5]. Also included in Figure 8 are the axial load *vs* strain curve (with open circles representing data points) and the data at fracture, which are represented by the solid black circles at the large true strains (one circle for each fracture surface). These data were estimated from measurements of the fracture surface area and the final load level just prior to fracture. A dashed line was drawn to approximately connect these data points to the point at which curve 3 achieved its constant slope. The axial load curve is shown to illustrate the onset of diffuse necking (at the maximum axial load level). Figures 8(b) and (c) are secondary electron images of one GMT #34 fracture surface, with the latter showing that microvoids were more or less uniformly distributed.

Figure 9(a) shows a similar set of five curves using a miniature tensile bar with a square cross section. Overall, the tensile stress-strain behaviors of the two base material tensile bar geometries are rather similar, although the stress level of the miniature square tensile bar is slightly lower. In addition to some experimental variations (*e.g.*, different load cells, one from the MTS universal materials testing machine and another from the desktop mini-tensile tester), the lower stress level may also be due to a slight overestimate of the cross-
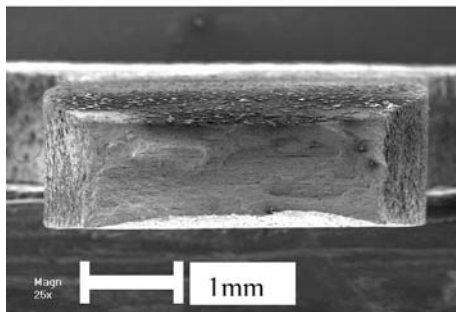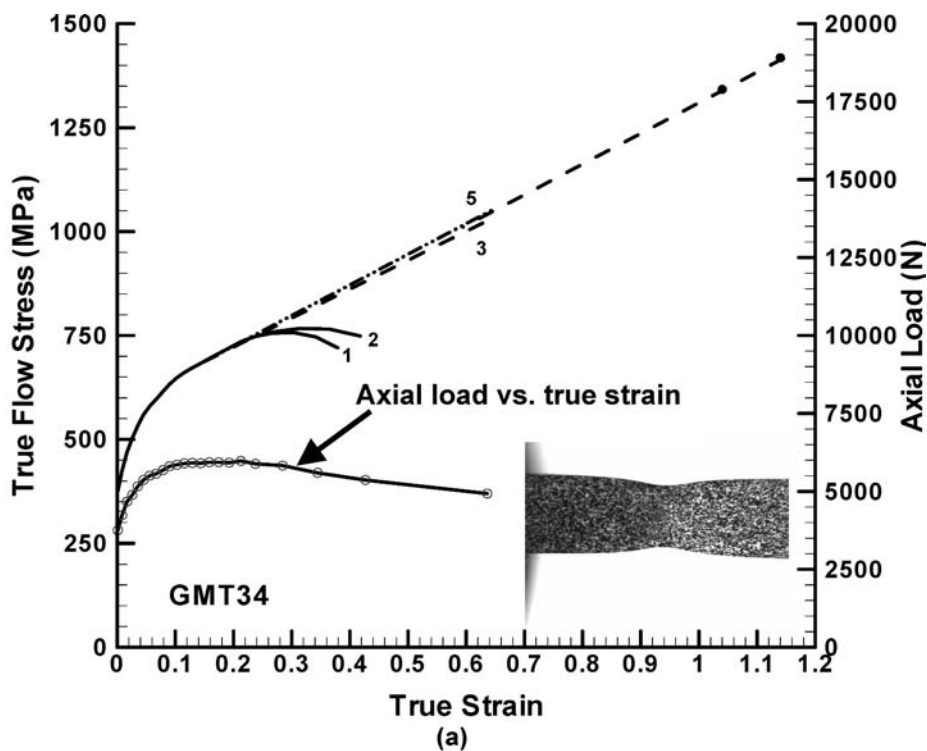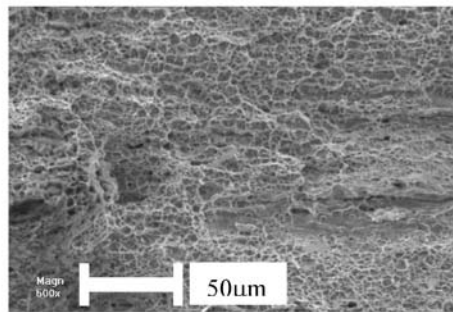
Fig. 8—(a) The axial load *vs* true strain $\bar{\varepsilon}_1^{(5)}$ (open circles) for GMT #34 (base material), using a compact tensile bar with a rectangular cross-section 5 × 2 mm². Curves 1, 2, 3, and 5 are the measured uniaxial tensile stress-strain curves according to Eq. [1], using the four axial true strain measures, $\bar{\varepsilon}_1^{(1)}$, $\bar{\varepsilon}_1^{(2)}$, $\bar{\varepsilon}_1^{(3)}$, and $\bar{\varepsilon}_1^{(5)}$, defined in Eqs. [2] through [5] and illustrated in Fig. 4(a). The solid circles are the estimated fracture stresses and strains based on the complementary fracture surface areas and the final load at rupture. The estimated true stress and strain at failure are 1418 MPa and 114 pct (Table II). (b) and (c) secondary electron images of one fracture surface at 25 and 500 times magnifications, respectively. A digital image of the necked compact tensile bar is also shown as the inset in (a).

sectional area of the miniature tensile bars. The as-machined surfaces of the miniature tensile bars appeared to be slightly rough; this could influence the accuracy of their measured cross-sectional area (their cross-sectional area was about 0.25 mm², which is 1/40 of the cross-sectional area of the larger rectangular tensile bars). On the other hand, the square tensile bars showed a more gradual development of diffuse necking, although the onset strains of diffuse necking were similar in both types of tensile bars: the difference between curves 1 and 2 is much larger in Figure 9(a) than in Figure 8(a). The tapering-off and softening of curves 3 and 5 in Figure 9(a) is indicative of the insufficient spatial resolution of the strain-mapping measurements as the diffuse necking evolved towards localized necking and ductile rupture. Figures 9(b) through (e) are secondary electron images of both

of the GMT #92 fracture surfaces. Again, this base material tensile bar exhibited a dimpled fracture surface where microvoids were more or less uniformly distributed. No evidence of failure initiation was observed at the edges or the surfaces of the miniature square tensile bars that were EDM machined from the base metal.

2. Simulated heat-affected zones

Figures 10 and 11 summarize the tensile testing results and fracture surface characteristics of the representative soft GMT #77 and hard GMT #76 heat-affected zone miniature tensile bars. Note that the true stress of the hard heat-affected zone of GMT #76 (Figure 11(a)) was nearly twice that of the base materials (Figures 8(a) and 9(a)) before diffuse necking. However, the plastic response of the soft heat-affected
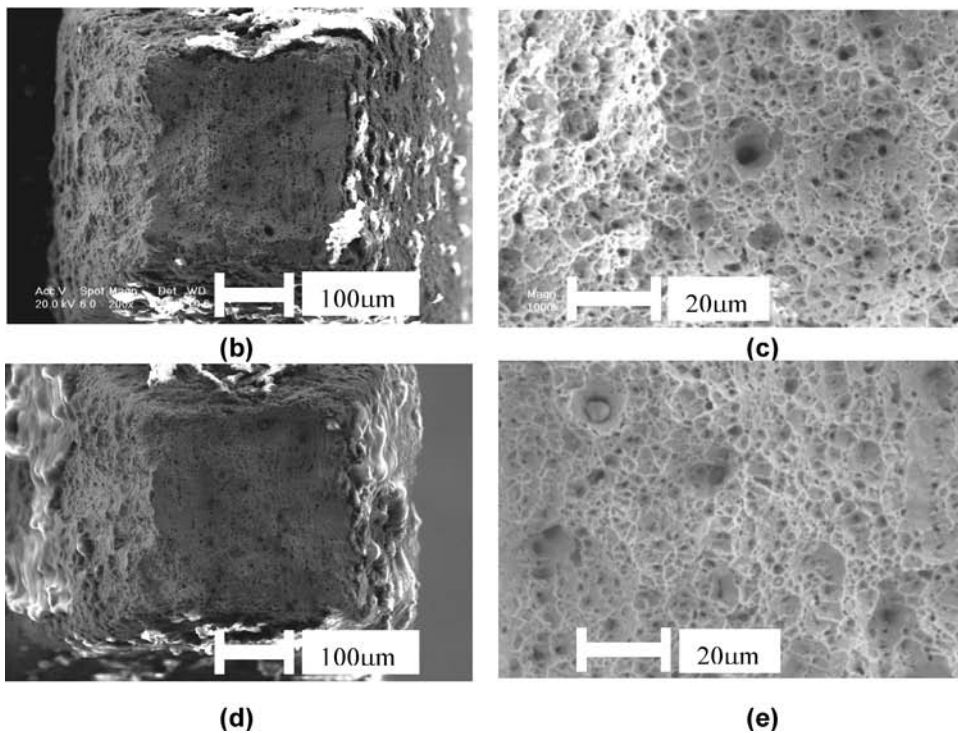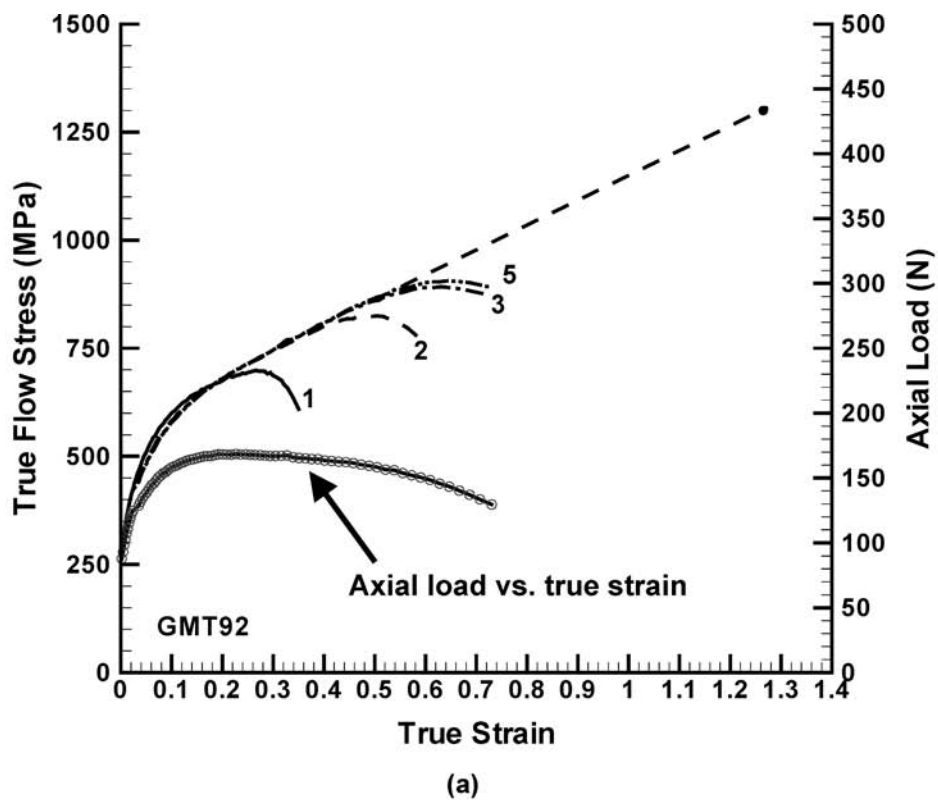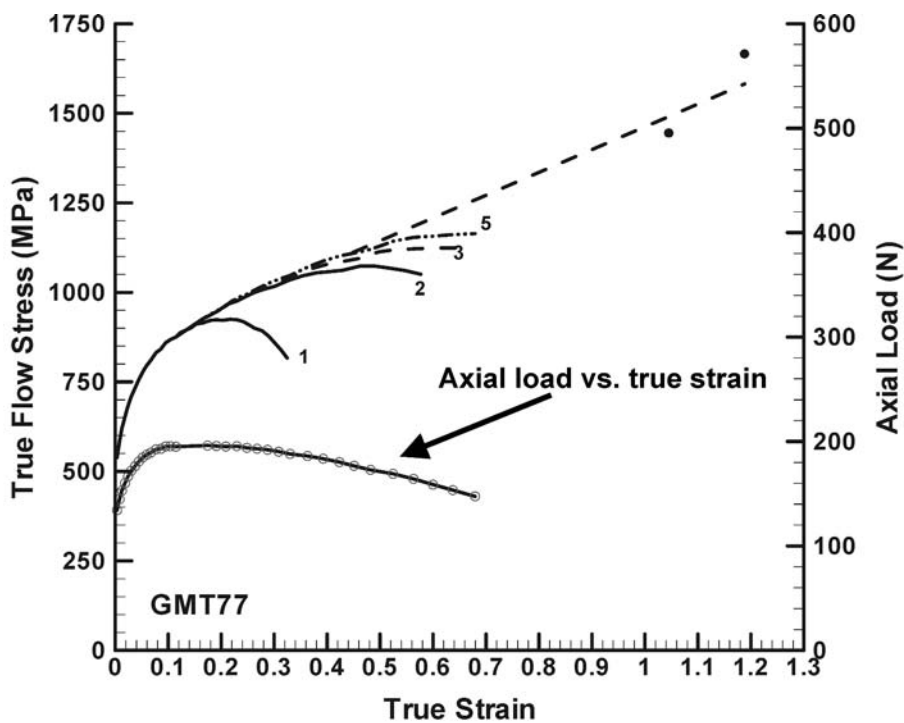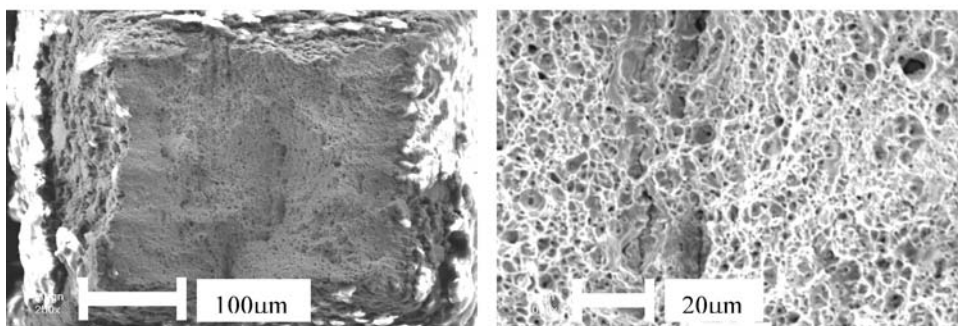
Fig. 9—(a) Summary of the tensile test results for GMT #92 (base material), using a miniature tensile bar with a cross-section 0.5×0.5 mm² square. (b) through (e) Secondary electron images of the two matching fracture surfaces (the magnifications of (d) and (e) are 200 and 1000 times, the same as those of (b) and (c), respectively).

zone shown in Figure 10(a) for GMT #77 was intermediate to that of the hard heat-affected zone and base materials, but certainly closer to that of the base material. As seen in Table II, the YS and UTS of the soft and hard heat-affected zones were, on average, 473 and 651 MPa, and 1273 and

1464 MPa, respectively. Compared to the soft heat-affected zone, the hard heat-affected zone exhibited a smaller strain-hardening rate. A large variation was also noted in the engineering strains at the UTS, for which a strain of 23 pct was recorded for the soft heat-affected zone, compared to a strain

Fig. 10—(a) Summary of the tensile test results for the miniature tensile bar GMT #77 (soft heat-affected zone) and (b) through (c) secondary electron images of one fracture surface at two different magnifications (250 and 1000 times).

of 5.3 pct for the hard heat-affected zone. Furthermore, the strains at the onset of localized necking and at fracture appeared to be somewhat larger for the soft heat-affected zone. For instance, strains at the onset of localized necking were between 50 and 70 pct for the hard heat-affected zone and about 70 pct or more for the soft heat-affected zone. Unlike the strains at the onset of localized necking, the strains at fracture were considerably more different; they averaged 84 pct for the hard heat-affected zone, as compared to 141 pct for the soft heat-affected zone. Note that the estimated fracture stresses were, on average, 1554 and 2006 MPa, for the soft and hard materials, respectively (Table II).

Figures 10(b) and (c) for the soft heat-affected zone (GMT #77) show regular dimples (in one fracture surface) with sizes similar to those found in the base material. The smaller dimples of the soft heat-affected zone and the base materials can be linked to the slightly higher ductility observed in the softer

microstructures. Figures 11(b) and (c) show one fracture surface of the hard heat-affected zone (GMT #76). The SEM images reveal that the fracture was somewhat ductile, as indicated by numerous microvoids, or dimples, and several larger voids (20 to 40 μm in diameter). Since quasi-cleavage-like features were also detected (Figure 11(c)), a component of the deformation could be characterized as brittle. Brittle fracture at ferrite-martensite boundaries is conceivable and would perfectly substantiate the directionality in the fracture observed in Figure 11(c), where an entire grain appears to be missing.

3. Weld fusion zone

Based upon DIC analyses of all tensile testing data for 13 fusion zone tensile bars, the results depicted in Figures 12(a) through (c) were selected as being representative of a weld fusion zone of good quality. Figure 12(a) shows true stress-true strain curves for the fusion zone bar GMT #28, with the strain
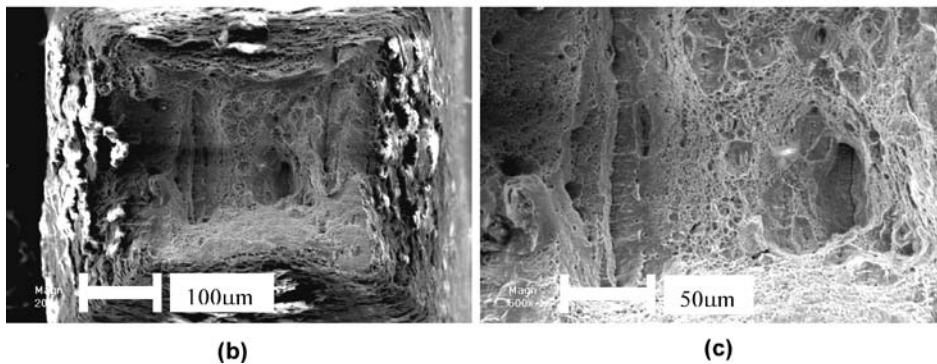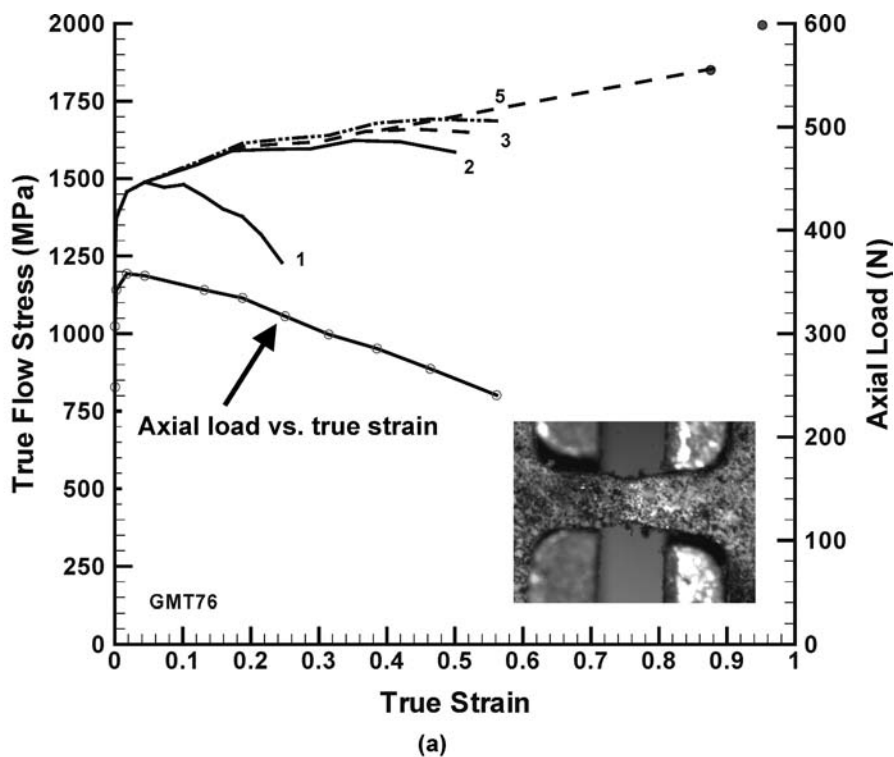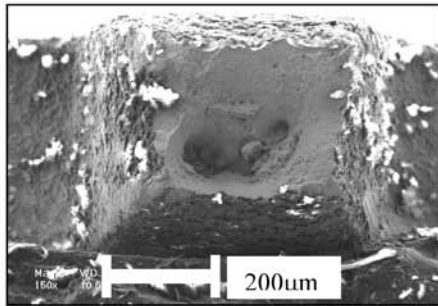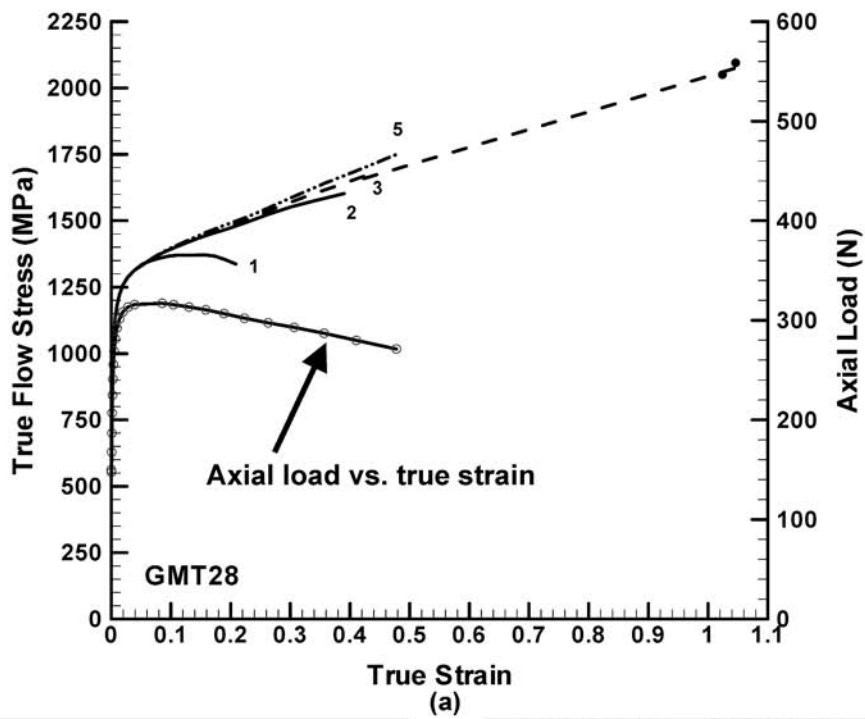
Fig. 11—(a) Summary of the tensile test results for the miniature tensile bar GMT #76 (hard heat-affected zone) and (b) through (c) secondary electron images of one fracture surface at two different magnifications (200 and 500 times). A digital image of the necked miniature tensile bar is also shown as the inset in (a).

range being extended up to the fracture point, which is marked by the solid black circles at the end of the dashed line. The maximum load, which indicates the onset of diffuse necking in conventional tensile testing, was reached at a plastic strain of about 6.4 pct (Table II, GMT #28). Note that curves 2 and 3 are bounded by curves 1 and 5, and a weak but linear strain-hardening rate is observed beyond diffuse necking. The onset of localized necking occurred (approximately) at a true strain of 45 pct or higher, based on curve 3. Note that fracture occurred at approximately 103 pct strain, when the flow stress reached 2073 MPa (error estimates were ±15 to 25 pct for both quantities). Curve 3 was linearly extrapolated to the fracture point and the extension represents the best estimate of the true stress-strain behavior of GMT #28 to failure. Overall, the stress-strain curve of the good fusion weld zone is similar to that of the hard heat-affected zone described earlier.

The topography of the fracture surfaces also exhibited some noteworthy features, as observed in the secondary elec-tron images of Figures 12(b) through (e). Note that Figures 12(b) and (c) represent one fracture surface, while its com-plement is shown in Figures 12(d) and (e). A large ellip-soidal void (about 200 μm in length) is seen near the center of the tensile bar cross-section of GMT #28. Shrinkage voids and microscopic cracks, which are not unusual in resistance spot welds of dual-phase steels, could in fact be responsi-ble for the fracture morphology depicted in Figures 12(b) through (e). Alternatively, if the void shown in these fig-ures did not result from defects induced by welding, but grew instead from the coalescence of microvoids, the most significant void growth is likely to have occurred between localized necking and final fracture. Given that negligible void growth occurred between the onset of diffuse and local-ized necking, then the underlying assumption of volume con-servation during plastic deformation in Eq. [1] is reasonable. Despite defects within the fusion zones, the tensile response of GMT #28 was typical of those weld fusion zones that
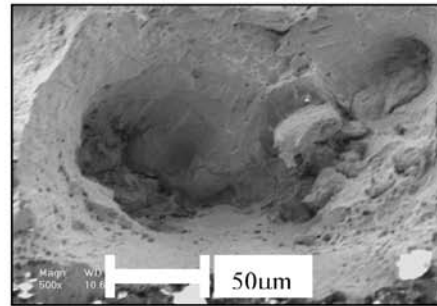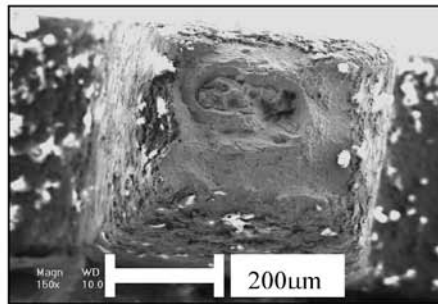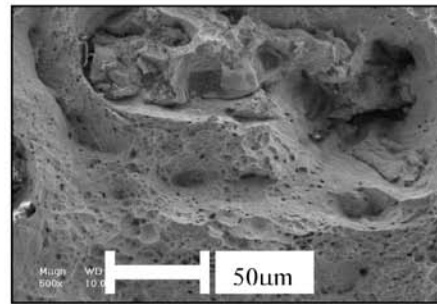
Fig. 12—(a) Summary of the tensile test results for the miniature tensile bar GMT #28 (good weld fusion zone, failed by typical diffuse and localized necking). (b) through (e) secondary electron images of the two matching fracture surfaces at two different magnifications (150 and 500 times).

failed *via* necking and rupture (Table III). The numerous microvoids, or dimples, observed all around the abnormal regions of both GMT #28 fracture surfaces indicate that deformation was primarily ductile until final rupture. Still, this ductility may appear surprising, as typical martensitic microstructures in weld fusion zones are known to be brittle. On the other hand, the ductile features seen in the frac-

ture surface are consistent with the behavior depicted in the true stress-true strain curves.

D. *Plastic Response with Defective Weld Fusion Zones*

Table III shows that 8 of the 13 miniature tensile bars for the fusion zone (*i.e.*, GMT #21, #24, #25, #28, #29, #30,

#31, and #80) failed after substantial diffuse necking in the gage section. As shown in Table II, the true strains at fracture exceeded 100 pct. On the other hand, the five remaining fusion zone miniature tensile bars (*i.e.*, GMT #23, #26, #27, #78, and #82) failed at much smaller strains, a characteristic that was unexpected.

Figure 13 shows uniaxial stress-strain curves for GMT #78. This tensile bar exhibited the representative characteristics of premature fracture in tension. Its defective nature precluded meaningful application of Eqs. [1] through [5], and the associated stress-strain behavior in Figure 13 is strictly qualitative. Note the small fracture strain (estimated in Table II as 25 pct) and the considerably reduced flow stress at fracture (654 MPa). These unexpected tensile testing results for GMT #78 are further explored in Figures 14(a) through (g). Figures 14(a) through (c) are deformation maps generated by image correlation at $F = 240.0\ N$. Four secondary electron images of one fracture surface are given in Figures 14(d) through (g) (at progressively higher magnifications). The top image set (Figure 14 (a)) shows the axial displacement (left panel), u, and the transverse displacement (right panel), v, in millimeters. The true axial (Er1) and transverse (Er2) strain contour levels are shown in the left and right panels, respectively, of Figure 14(b). The shear strain and in-plane rigid rotation contours are shown in the left and right panels, respectively, of Figure 14(c). These contour maps were recorded just prior to the complete fracture of GMT #78. The axial strain distribution is certainly not representative of the typical symmetric necking process that precedes rupture, as shown, for example, in Figure 4(a). Most interestingly, the contours of axial and transverse strain in Figure 14(b) are very similar to strain fields that can be computed (or measured) from a crack tip or notch growing from the tensile bar edge across the gage section under tension.[23,24] Two arrows have been drawn to connect the axial strain map in the left panel of Figure 14(b) with the left surface (labeled L) in Figure 14(d), to point out that this was the tensile bar surface from which the deformation maps in Figures 14(a) through (c) were generated. Figure 14(c) shows that the shear strains were greatest near the surface of the
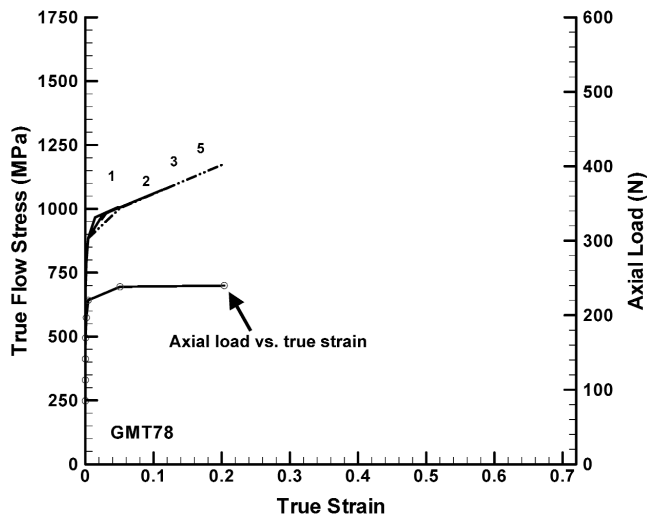
crack tip in Figure 14(d), while the opposite surface of the gage section experienced the largest rotations, as shown in the right panel of Figure 14(c).

The four secondary electron micrographs in Figures 14(d) through (g) revealed unusual features. The upper left image shows an overall view of the fracture surface, while Figures 14(e) through (g) provide progressively higher magnification views of details seen across this fracture surface. Figures 14(e) and (f) show the typical dendritic solidification microstructure that normally develops in undercooled alloys. These characteristics are highly unusual for low-alloy steels. First and foremost, the dendritic morphology suggests that the material was pulled apart while still liquid. Normal shrinkage could explain such a defect, but it is unclear whether it could cause such a large array of interdendritic cracks covering a substantial portion of the tensile bar cross section (Figure 14(d)). These cracks were as large as the tensile bar widths and they appear to be the underlying cause for the premature fracture observed in 5 of the 13 fusion zone tensile bars. Interactions with irregularities at the specimen surface may also have caused the material to deform more from the edges, as observed in the accompanying strain maps in Figures 14(a) through (c).

Insufficient welding current levels and hold times are possible causes for weld cracking, as all five of the tested fusion zone coupons with defective welds were welded at current levels of 9 and 9.5 kA. A fundamental mechanism responsible for pre-existing cracks before tensile testing may also be related to the steel chemical composition. When alloying elements partition from the solid-iron δ-ferrite phase, the freezing range is often increased, and in some cases interactions between alloying elements lead to the formation of low-melting point constituents, which segregate to dendrite boundaries.[4] When tensile stresses accumulate in this microstructure during solidification (ostensibly from solidification shrinkage), resistance to cracking usually decreases. A cursory examination of the secondary electron images in Figures 14(e) and (f) reveals the presence of unknown microconstituents represented by the spherical particles of widely different sizes. The particle morphology is shown in greater detail in Figure 14(g). These particles, which appeared to be slightly brighter than iron in the secondary electron images, are likely less conductive than the ferrous matrix. Their spherical morphology, which results from the fact that they do not wet on the ferrous phase or anywhere else, indicates that their surface free energy (*e.g.*, surface tension) is high, particularly compared to that of iron. Both the reduced conductivity and spherical morphology of these new microconstituents suggest that they are semimetallic. Furthermore, based upon a surface energy assessment, it may be concluded that some of these particles may possess a much greater melting temperature than iron.

To further investigate the spherical particles in Figure 14(g), chemical compositions were measured on several selected particles by energy-dispersive spectroscopy. Due to prolonged exposure to air, elements such as oxygen and nitrogen were removed from the quantitative analysis, as they could have resulted from contamination after fracture occurred. While nitrogen was virtually absent, oxygen was found in significant but unknown concentrations. Of the ten particles that were analyzed, the results of four particles, denoted as 1N, 2N, 1S, and 2S, are shown in Figures 15(a) through (e). These particles are shown at a higher magnification in the secondary electron images in the left panels of Figures 15(b) through (e). The

Fig. 13—Summary of the tensile test results for the miniature tensile bar GMT #78 (poor weld fusion zone, failed prematurely by edge cracking).
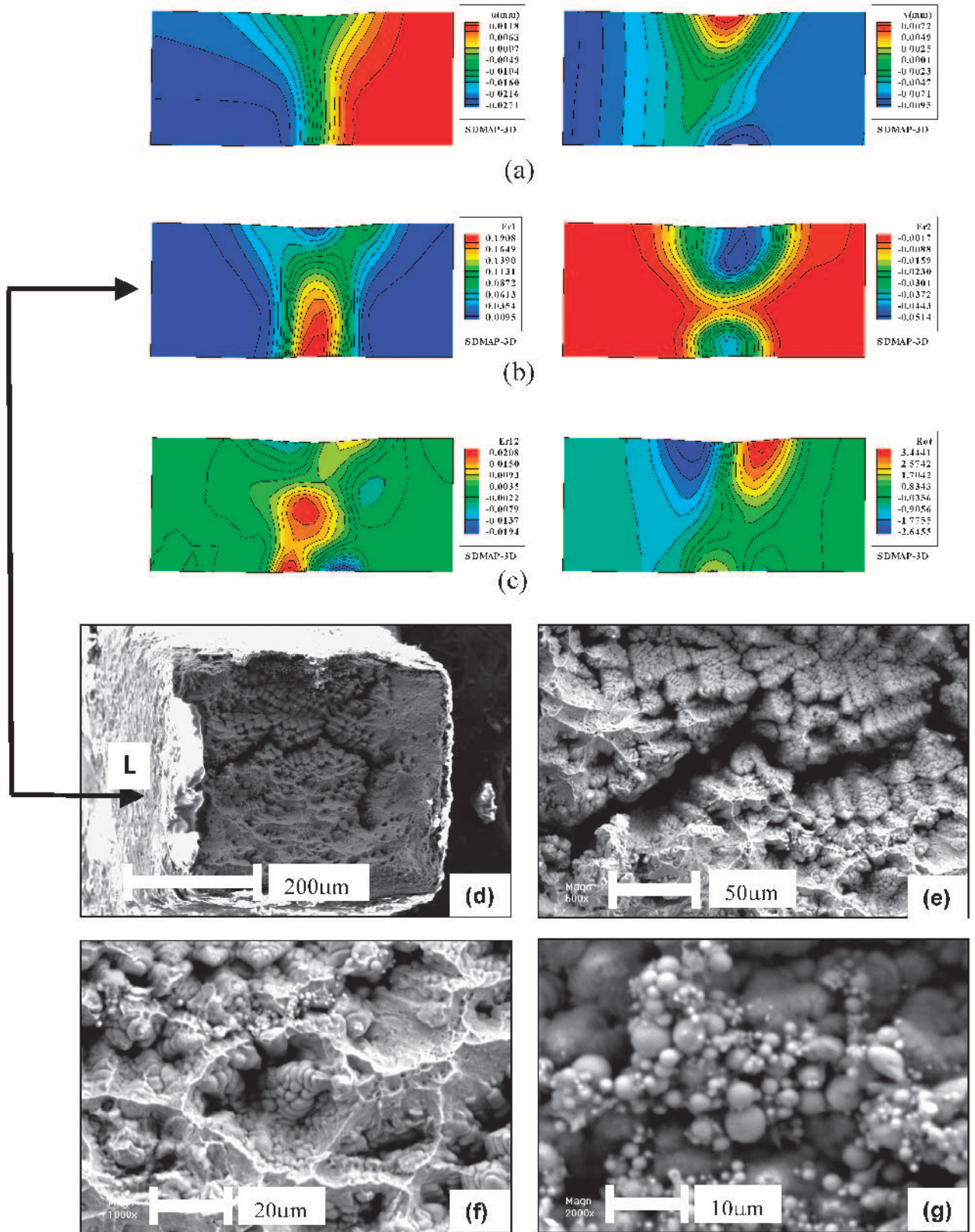
Fig. 14—(a) Displacement contour maps: axial (left) and transverse (right). (b) Strain contour maps: axial (left) and transverse (right). (c) Additional contour maps: shear strain (left) and in-plane rigid rotation (right). (d) through (g) Scanning secondary electron microscropy images at magnifications of 100, 500, 1000, and 2000 times, respectively, of one fracture surface of bar GMT #78.

results from compositional analyses based on energy-dispersive spectra data are shown in the tables to the right of Figures 15(b) through (e), with breakdowns of the chemical constituents by atomic weight percent. Light metal elements (e.g., sodium, magnesium, and aluminum) were found in the weld, along with silicon and copper. Recall that silicon is an alloying
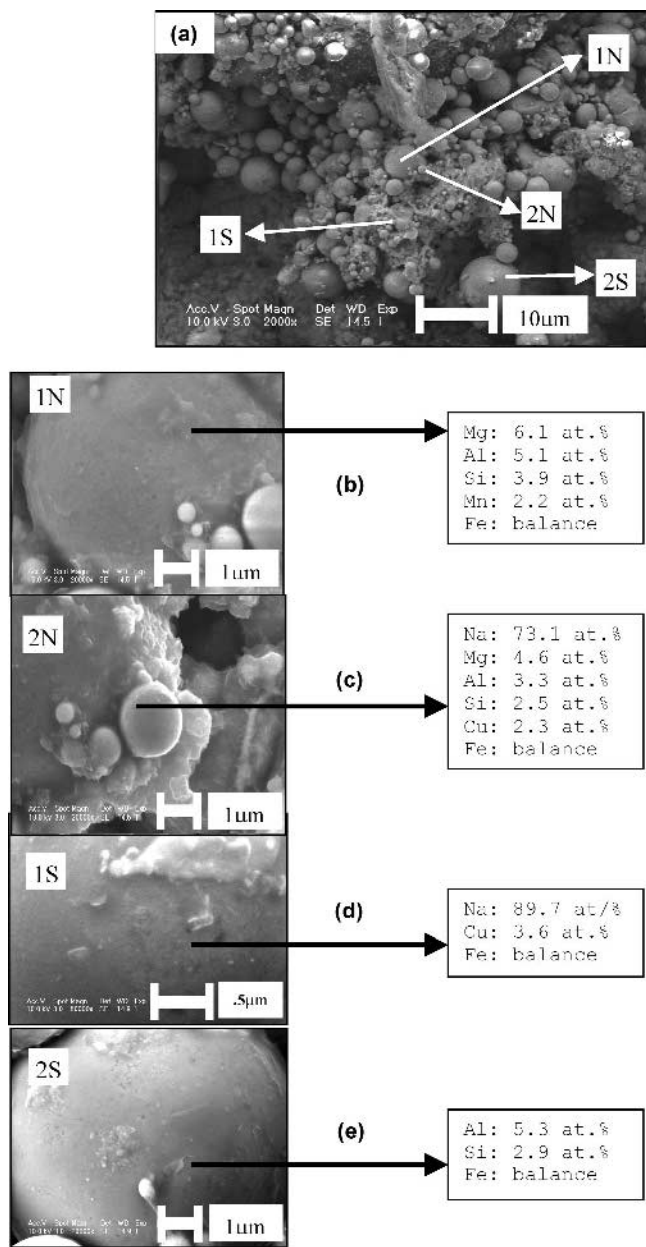
Fig. 15—(*a*) through (*e*) Secondary electron images accompanied by corresponding chemical compositions based on energy-dispersive spectra analyses. (b) through (e) Magnified views of selected sampling areas in (a).

element in dual-phase steel (Table I) and that its presence was not entirely unexpected. In contrast, the presence of alkaline and alkaline earth metals was not anticipated. These elements, together with silicon, are commonly used for slags (glassy phases), because they are strong deoxidizers and desulfurizers used in steel making, as can be explained by their electronegativity values, which are significantly different from those of oxygen or sulfur. In all likelihood, these light elements interacted with the oxygen that was dissolved in liquid iron to form semimetallic inclusions like oxides, as also suggested by the glassy appearance of several particles. Because semimetallic particles such as oxides are stable at elevated temperatures, it also appears likely that some of the particles formed while the ferrous phase was still liquid. As a result, some particles would have been gradually pushed by the

advancing solidification front. This possibility would justify the reason that several particles have heterogeneous chemical compositions and exhibit different layers, as if they had grown from smaller particles. In principle, particles made of the alkaline metals are the most stable, as proven by Ellingham diagrams.[26] These light particles can be expected to grow to a larger extent, provided that light elements are present in sufficient concentrations and the growth rates are sufficiently fast. The inset tables from the energy-dispersive spectra data in Figures 15(c) and (d) confirm that some of the largest particles were indeed made of sodium (a possible source of Na may be the Zn bath used in making the galvanized dual-phase steel material). Regardless of the formation sequence of these particles, it can be concluded that they increased the susceptibility of the welded dual-phase steel to cracking, causing normal shrinkage to induce more and longer interdendritic cracks. The contamination of the dual-phase steel by these elements thus appeared as a major factor in explaining some of the premature fractures observed in the weld fusion zones and shown in the strain maps of Figures 14(a) through (c).

IV. CONCLUDING REMARKS

Quasi-static, uniaxial tensile stress-strain curves of as-received dual-phase steels, resistance-spot-weld heat-affected zones, and fusion zones were successfully measured up to the onset of localized necking, using miniature tensile bars and a novel strain-mapping technique based upon DIC. The DIC technique was essential for extracting the stress-strain relationships of the miniature tensile bars with resistance-spot-weld microstructures, well beyond the onset strain level of diffuse necking (*i.e.*, about 6 pct strain for weld fusion zones and simulated heat-affected zones). Compared to the initial ferrite + martensite microstructure, the weld fusion zone (mostly composed of martensite) exhibited far greater flow stresses, smaller strain-hardening rates, significantly smaller strains at the onset of diffuse necking, and also, quite surprisingly, comparable strains at fracture. Fracture strains regularly exceeded 100 pct in the absence of major defects. Despite significant strengthening, weld fracture surfaces exhibited characteristics typical of ductile failure. In about a third of the miniature tensile bars machined from weld fusion zones, and only in these samples, fracture initiated within the gage section edges. While surface irregularities might be the source of this behavior, the edge cracking was mainly attributed to subsurface defects caused by welding (shrinkage or solidification cracking). At locations where decohesion along dendritic interfaces was observed, energy-dispersive spectroscopy revealed the presence of contaminants such as sodium, magnesium, aluminum, silicon, and copper. Two types of simulated heat-affected zones (soft *vs* hard) were identified, depending on whether they were comparable in plastic deformation to the base material or the weld fusion zones. The fact that heat-affected-zone tensile bars exhibited a range of mechanical properties was supported by nanoindentation measurements across weld cross sections.

REFERENCES

1. *Technical Transfer Dispatch #6 (Body Structure Materials)*, ULSAB-AVC Consortium, American Iron and Steel Institute, Southfield, MI, May 26, 2001.
2. G. Krauss: *Steels—Heat Treatment and Processing Principles*, ASM INTERNATIONAL, Materials Park, OH, 1990, pp. 247-79.
3. P.K. Ghosh, P.C. Gupta, P. Ramavtar, and B.K. Jha: *Welding J.*, 1991, vol. 70 (1), pp. 7s-14s.
4. *ASM Handbook*, vol. 6, *Welding, Brazing and Soldering*, ASM, Materials Park, OH, 1993.
5. *Welding Handbook*, 8th ed., L.P. Connor, ed., American Welding Society, Miami, FL, 1987.
6. P.K. Gosh, P.C. Gupta, P. Ramavtar, and B.K. Jha: *Iron Steel Inst. Jpn. Int*., 1990, vol. 30 (3), pp. 233-40.
7. R.W. Rathbun, D.K. Matlock, and J.G. Speer: *Welding J.*, 2003, vol. 82 (8), pp. 207s-218s.
8. L. Devilliers, D. Kaplan, and P.S. Saint-Martin: *Soudage Techniques Connexes*, 1986, vol. 40 (11–12), pp. 387-95.
9. T. Saito and Y. Ichiyama: *Welding Int*., 1996, vol. 10 (2), pp. 117-23.
10. *Weldability of High Tensile Strength Steel Sheets*, Sumitomo Metals Industries, Ltd. (5-33 Kitahama 4-chome, Chuo-ku, Osaka 541-0041, Japan), private communication, 2002.
11. S.M. Zuniga and S.D. Sheppard: *Modeling Simul. Mater. Sci. Eng.*, 1995, vol. 3 (3), pp. 391-416.
12. J.F. Zarzour, P.J. Konkol, and H. Dong: *Mater. Characterization*, 1996, vol. 37, pp. 195-209.
13. E. Markiewicz, P. Ducrocq, P. Drazetic, G. Haugou, T. Fourmentraux, and J.Y. Berard: *Int. J. Mater. Product Technol*., 2001, vol. 16 (6–7), pp. 484-509.
14. D. Tabor: *Hardness of Metals*, Clarendon Press, Oxford, United Kingdom, 1951.
15. W.C. Oliver and G.M. Pharr: *J. Mater. Res*., 1992, vol. 7, pp. 1564-83.
16. N. Zhang, C. Xie, and W. Tong: *Mater. Res. Soc. Symp. Proc.*, 2004, vol. 782, pp. A6.3.1-A6.3.6.
17. E. Nakayama, K. Okamura, M. Miyahara, M. Yoshida, K. Fukui, and H. Fujimoto: *J. Soc. Automotive Eng. Jpn*., 2003, Oct., pp. 313-18.
18. W. Tong: "A User's Guide to the Yale Surface Deformation Mapping Program (SDMAP)," Technical Report, Yale University, New Haven, CT, 1996–2004.
19. B.W. Smith, X. Li, and W. Tong: *Exp. Technol*., 1998, vol. 22 (4), pp. 19-23.
20. W. Tong and N. Zhang: *Proc. ASME Manufacturing Engineering Division*, MED- 2001, vol. 12.
21. W. Tong: *Exp. Mech*., 1997, vol. 37 (4), pp. 452-59.
22. W. Tong: *J. Mech. Phys. Solids*, 1998, vol. 46 (10), pp. 2087-2102.
23. W. Tong, H. Tao, and N. Zhang: *Mater. Res. Soc. Symp. Proc*., 2004, vol. 785, pp. D7.7.1-D7.7.6.
24. W. Tong: *Exp. Technol*., 2004, vol. 28 (3), pp. 63-67.
25. N. Zhang, H. Tao, and W. Tong: *Int. J. Mech. Mater. Design*, 2004, submitted for publication.
26. O.F. Devereux: *Topics in Metallurgical Thermodynamics*, Krieger Publishing Company, Malabar, FL, 1989, p. 86.